Determination of Elastic Moduli of Thin Layers of Soft Material Using the Atomic Force Microscope

Emilios K. Dimitriadis,* Ferenc Horkay,[†] Julia Maresca,[‡] Bechara Kachar,[§] and Richard S. Chadwick[‡]

*Division of Bioengineering and Physical Science, Office of Research Services, Office of the Director; [†]Section on Tissue Biophysics and Biomimetics, Laboratory of Integrative and Medical Biophysics, National Institute of Child Health and Human Development; and [‡]Section on Auditory Mechanics, and [§]Section on Structural Cell Biology, National Institute of Deafness and Other Communication Disorders, National Institutes of Health, Bethesda, MD 20892 USA

ABSTRACT   We address three problems that limit the use of the atomic force microscope when measuring elastic moduli of soft materials at microscopic scales. The first concerns the use of sharp cantilever tips, which typically induce local strains that far exceed the linear material regime. We show that this problem can be alleviated by using microspheres as probes, and we establish the criteria for their use. The second relates to the common use of the Hertz contact mechanics model, which leads to significant errors when applied to thin samples. We develop novel, simple to use corrections to apply for such cases. Samples that are either bonded or not bonded to a rigid substrate are considered. The third problem concerns the difficulty in establishing when contact occurs on a soft material. We obtain error estimates for the elastic modulus resulting from such uncertainty and discuss the sensitivity of the estimation methods to error in contact point. The theoretical and experimental results are compared to macroscopic measurements on poly(vinyl-alcohol) gels.

INTRODUCTION

Knowledge of mechanical properties of cells and other biological tissues at high resolution could be instrumental to understanding how mechanical interactions affect function. The atomic force microscope (AFM) used as a microindenter has recently emerged as a mainstream microrheology tool used for this purpose (Vinckier and Semenza, 1998; Hoh and Heinz, 1999). In addition to shedding light onto function, mapping the distribution of elastic properties across imaged areas may also be used to correct topographic images for deformations caused by the imaging forces themselves (Hoh and Heinz, 1999).

The use of the AFM as a microindenter to measure elastic properties and other surface interaction forces was introduced early in its development (Burnham and Colton, 1989). Such measurements on biological tissues followed soon after (Tao et al., 1992; Radmacher et al., 1992). In these applications, "force–displacement" curves are collected with the AFM and used in conjunction with appropriate mathematical models describing the mechanics of contact to estimate the Young's modulus and other material properties or structural parameters (Radmacher et al., 1994, 1996; Heuberger et al., 1994; Radmacher, 1995; Rotsch et al., 1997; Sato et al., 2000; Haga et al., 2000; Mahaffy et al., 2000). In these and other publications, with the exception of the recent work attaching spherical beads to the AFM cantilevers (Mahaffy et al., 2000), standard commercial canti-

levers were used with pyramidal tips having tip radii of curvature of the order of tens of nanometers. Sample thickness typically varied from several microns to less than one micron, and they were supported on relatively rigid substrates, such as glass or mica. In all cases, force–displacement data were analyzed by fitting them with Hertzian models of contact in which two major assumptions are made: linear elasticity and infinite sample thickness. Both assumptions, however, can lead to significant errors. Another difficulty associated with these measurements is the fact that the initial contact point is difficult to establish with soft samples. Also, imperfections in commonly used cantilevers with pyramidal tips may result in an ill-defined contact-region geometry, which introduces uncertainty in choosing the appropriate fitting model. These issues are addressed in this paper.

Some of the problems have been highlighted in the literature, where it has been shown, depending on the applied force and on the sample thickness, that large errors may result when using infinite thickness models (Kim, 1996; Domke and Radmacher, 1998; Akhremitchev and Walker, 1999). In the latter, the authors used the theoretical models of Dhaliwal and Rau (1970) to compute force-displacement curves for finite sample thickness to show that, for soft, thin samples the error in the estimated elasticity modulus can be an order of magnitude. More recent finite element modeling of the contact problem (Costa and Yin, 1999) pointed out that finite deformations occur in soft samples when probed by the usual cantilevers carrying sharp pyramidal tips, and that significant errors may occur when using models derived from linear elasticity. Mahaffy et al. (2000) attached microspheres to the cantilevers to avoid damaging delicate biological samples and they showed that, with thick gel samples, good agreement can be obtained with macroscopic measurements of the same material. On both thick and thin

---

samples, they showed the apparent Young's modulus as computed using the Hertz model, remains constant over some range of applied force. As will be discussed here, however, that approach may introduce artifacts that cannot be addressed in the context of the Hertz theory. Other efforts have proposed using relative stiffness measures (A-Hassan et al., 1998), or evaluating relative Young's moduli based on comparisons with well-known materials (Reynaud et al., 2000). In both cases, however, the need for a model at the outset describing the relation between force and indentation is not eliminated.

The general problem of contact between isotropic elastic bodies has been studied for over a century starting with the well-known works of Hertz (1881) and Boussinesq (1885). Their work resulted in simple explicit expressions for the force-indentation relation for an infinitely thick sample. During the last few decades, improved mathematical tools and strong interest in the materials science and mechanics communities produced extensive literature on the subject. Landau (Landau and Lifshitz, 1959) summarized the Hertzian approach, re-derived his results, and gave expressions for both stress and displacement fields. Sneddon (1951, 1965) followed the approach taken by Boussinesq and developed a methodology based on integral transforms. He derived solutions for several axisymmetric indenter geometries, but solved the problem for infinitely thick samples only. Until now, calculations for the finite thickness layer have required extensive numerical computations, as exemplified in Tu and Gazis (1964), Popov (1962), and later in Dhaliwal and Rau (1970) and Chen and Engel (1972). Aleksandrov (1968, 1969) further developed the integral transform method and used asymptotic methods to solve the problem for a finite thickness layer. His final results, however, still require rather sophisticated mathematical manipulations. Moreover, his results are not valid for incompressible materials (Poisson's ratio $v = 0.5$), which is the case for most biological tissue. The numerical computations of Hayes et al. (1972) are valid for $v = 0.5$, and are the most appropriate to compare with the results of the present work, which also has no restrictions on the value of v. Matthewson's (1981) approximate analysis for very thin, bonded layers is also applied to incompressible materials. A rather important finding is that the force–indentation relation for very thin layers depends surprisingly strongly on whether the sample is bonded or not to the substrate (Yang, 1998; Chadwick, 2002). This should have important implications for biological samples where their attachment to substrates may not be well controlled.

In reviewing the literature on modeling the contact problem, it becomes clear that no convenient solutions exist for the indentation of finite thickness elastic samples. The reason lies in the intrinsic geometric nonlinearity whereby the actual contact area and hence the pressure profile depend on the total applied force. Existing mathematical formulations lead to an integral equation that has to be solved either numerically using finite element schemes or by other, rather complex computational schemes. This is a rather tedious and inconvenient approach for routine AFM use. Simpler, validated, analytical corrections to the infinite sample solutions, such as those developed here, should be very helpful. Our corrections are based on recasting the integral equations into a hierarchy of simpler integral equations that can be solved analytically.

The aims here are to: examine the limitations of the use of the widely available AFM cantilevers with their sharp tips but poorly defined tip geometry; further develop the use of microspheres as indenters; develop a simple-to-use theory that allows reliable determination of elastic moduli on soft samples irrespective of thickness, which are supported in different ways on rigid substrates; and verify the approach and the theoretical models by comparing results with those obtained from macroscopic measurements. Estimation of Young's modulus [N/m^2] instead of sample stiffness [N/m] is more desirable, because the latter depends on the experimental setup, as opposed to the former, which is an intrinsic material property that can be used to compute mechanical responses under any conditions.

MATERIALS AND METHODS

Microsphere attachment and cantilever calibration

Polystyrene microspheres (4- and 9.6-μm diameter, Interfacial Dynamics Corp., Portland, OR) were attached to the cantilever tips. The 9.6-μm spheres were attached to standard Si_3N_4 cantilevers (Digital Instruments, Santa Barbara, CA, nominal stiffness 0.06 N/m) adjacent to the existing pyramidal tip. The 4-μm spheres were attached to tipless cantilevers of the same nominal stiffness, obtained for this purpose (Digital Instruments). The attachment was effected using water-resistant, two-part epoxy adhesive using an inverted optical microscope and a micromanipulator. Calibration of the cantilevers was performed by first making a calibrated glass fiber cantilever of comparable stiffness that was then used to deflect the AFM cantilevers while measuring both the glass fiber vertical displacement and the vertical deflection at the contact point. The glass fiber was 50 μm in diameter and was pulled to a tip of $\sim$10 μm in a micro-pipette puller. The glass fiber calibration was performed by loading it with known weights close to its free end and measuring deflections. The measured stiffnesses were within 25% of the nominal value.

Gel composition and macroscopic shear modulus measurements

Poly(vinyl alcohol) (PVA) gels were prepared by cross-linking PVA ($M_w = 100,000$) in aqueous solutions with glutaraldehyde at pH = 1.5. Cross-links were introduced at different polymer concentrations. The molar ratio of the cross-linker to the monomer units of the polymer was 0.01 at all concentrations and this guaranteed that no swelling or shrinking of the gel would occur during or after the gelation process (Horkay and Nagy, 1980). 1 M HCl solution was used as a catalyst in all cases to adjust the pH.

Uniaxial compression measurements were performed by a TA.XT21 HR Texture Analyser (Stable Micro Systems, UK). This apparatus measures the deformation (± 0.001 mm) as a function of an applied force (± 0.01 N). Gel cylinders (height $\approx$ diameter $\approx$ 1 cm) equilibrated with pure water were deformed (at constant volume) between two parallel flat

glass plates. The shear modulus, G, was calculated from the nominal stress, σ (force per unit undeformed cross-section), using the equation,

$$\sigma = G(\Lambda - \Lambda^{-2}), \qquad (1)$$

where Λ is the macroscopic deformation ratio ($\Lambda = L/L_0$, L and L_0 are the lengths of the deformed and undeformed specimen, respectively). Eq. 1 applies to an isotropic, incompressible, neo-Hookean elastic material that has been shown to be appropriate for PVA gels (Horkay and Nagy, 1980). Measurements were carried out at deformation ratios $0.6 < \Lambda < 1$. No volume change or barrel distortion was detected. The shear modulus is simply related to the Young's modulus by $E = 2(v + 1)G$, which translates to $E = 3G$ for incompressible materials ($v = 0.5$). In all cases, fresh gels were made shortly before measurements were performed.

Gel preparation and electron microscopy

Thick ($\sim$2 mm) gel samples were made in petri dishes. Cubical gel sections 2 mm on the side were then quick-frozen by contact with a liquid nitrogen-cooled sapphire block of a Life Cell CF-100 quick-freezing machine (Research and Manufacturing Co., Tuscon, AZ) and promptly transferred into liquid nitrogen. The frozen gels were then fractured at $-150°C$ in a Balzers BAF301 freeze–fracture apparatus, etched for 10 min at $-100°C$, and rotary shadowed with platinum at 15° angle and backed with carbon at a 90° angle. Organic material was cleaned with 10% chromic acid. Replicas were observed and photographed on a Zeiss 902 transmission electron microscope in zero-loss imaging mode.

Figure 1 shows a representative image obtained from the above procedure. The image was taken on a fracture plane that laid parallel and very close to the gel-free surface and is, therefore, representative of the environment probed by the AFM tip. The gel consists of a rather homogeneous looking three-dimensional fiber network when observed at the scale of the image size. The mesh size of the cavities in most of the image area is distributed in the range between 30 and 90 nm with a mean of $\sim$65 nm. Occasional larger cavities appear, such as the apparent gaps of $\sim$0.15 μm in size observed in the image. The gel microstructure bears striking resemblance to known biological gelatinous tissue such as the supporting matrix of the otolithic membrane in the vestibular sensory apparatus of the frog (Kachar et al., 1990) and of the guinea pig (Lins et al., 2000).

Gel sample preparation for AFM and thickness measurement

For each polymer concentration, a relatively thick sample was made ($\sim$1 mm) and data were collected to ascertain the validity of the Hertz model and to explore the errors involved when using sharp tips. Thin samples were subsequently made of the same stock solution by the method described below. After cantilever calibration, the thickness of the gel was measured approximately by topographic AFM imaging of a 100×100-μm area that included the gel boundary. Regions $\sim$100 μm from the gel border were chosen, and a number of force-displacement curves were collected using three successive cantilevers (sharp, $R = 2$ and $R = 4.8$ μm).

Gel films were prepared that were firmly attached to the substrate and had a thickness of less than 5 μm. A small quantity of PVA solution (100–150 μl) containing the cross-linker and the catalyst was poured on silane, or polylysine-coated glass slides, held in vertical position to allow for the gel to drip down the slide aided by gravity. The slide was placed in a vibration-free environment and protected from drying by placing it in a saturated water vapor atmosphere. After the gel was fully formed, the thinnest part of the gel was found to have thickness between 1 and 4 μm as measured from the AFM topographic image. It was found that the gels adhered to the substrate well and that the step size could be measured
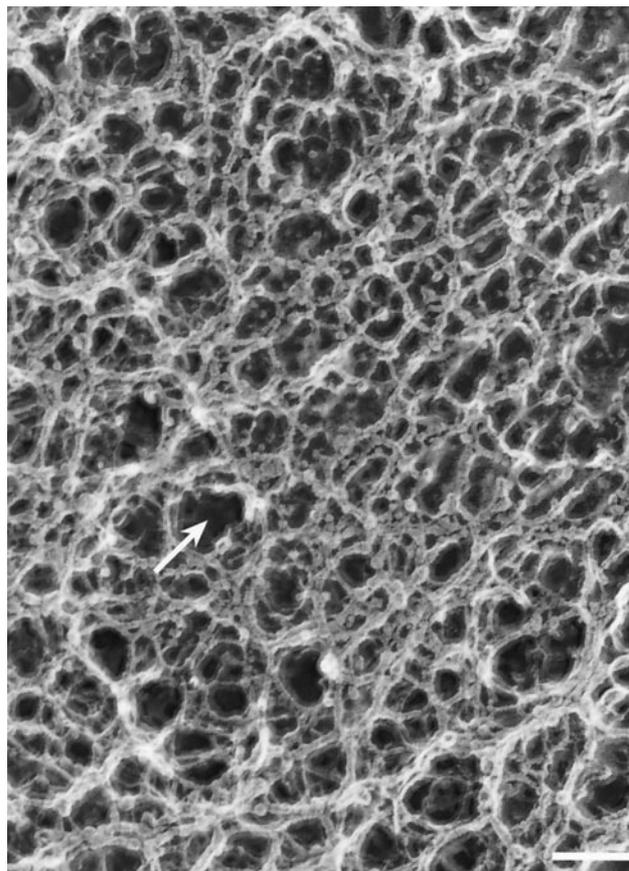

FIGURE 1 Transmission electron micrograph of PVA gel sample. Few large cavities (*arrow*) appear in an otherwise homogeneous matrix. Bar = 150 nm.

consistently under water using either the contact or the oscillating mode of the AFM. The resulting samples were fairly flat (rms fluctuation $\lesssim$ 25 nm). This type of sample is typical of single cells, and, at such sample thickness,
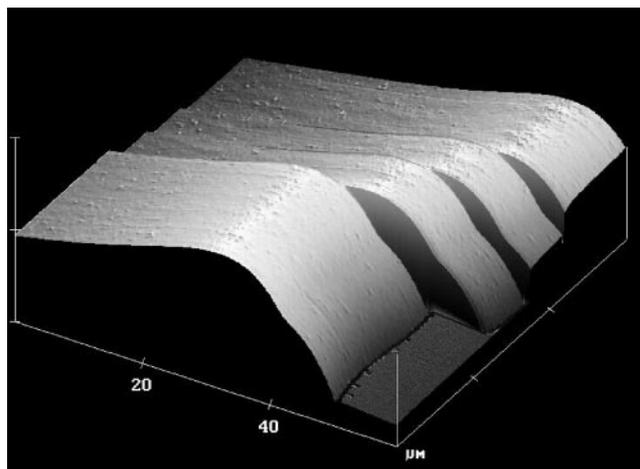

FIGURE 2 Topographic steps obtained using contact mode AFM imaging. Different strips indicate successive shifts in the scan region to view larger area of the gel. The vertical bar at the image front is 5 μm.

the Hertz theory of infinite half-space clearly breaks down. Figure 2 shows a typical thin gel step.

All samples were maintained in de-ionized water in which the measurements were also made using a commercial AFM (Bioscope, Digital Instruments) attached to an inverted optical microscope (Olympus IX-70). All force–displacement curves were collected using Si_3N_4 commercial cantilevers with nominal stiffness of 0.06 N/m.

Measurements and data analysis

Data collection was followed by visual truncation as close as possible to the contact point. The resulting data, within the error associated with the choice of the contact point, represent the deflection versus indentation relation. The data were often also truncated at high force so as not to exceed surface strains of ~10% as estimated by the Hertz theory when using attached microspheres. This was more difficult, however, when sharp tips were used because of the very high strains induced even by very small forces. In all cases, the gels were assumed to be incompressible ($v = 0.5$).

If the coordinates of the contact point are assumed, the linearity of the force–indentation relation with respect to E allows the inversion of any explicit model and the estimation of E for each data point independently. This is the method that is widely used and was also used here. An extension of the method solves the relevant model equations for the parameters by matching the data at a number of points equal to the number of parameters. The transcendental form of the finite thickness model complicates the inversion, which is not an insurmountable problem but would require some computational effort.

The method for parameter extraction used here fits the model to the complete set of data points by least squares method. Only those data points where contact is certain need be used and the complete set of unknown parameters can be optimally estimated. The small percentage of points corresponding to noncontact that may inadvertently be included will only have proportionally small effect. The nonlinearity of the model requires nonlinear regression analysis, which is available in many software packages. Here we used either the steepest descent or the Levenberg–Marquardt minimization algorithms available in Mathematica (Wolfram Research, Champaign, IL).

THEORY

In the following sections, the indentation geometry is first presented, followed by the conditions required for small strains, and finally by new theoretical models of the contact problem for finite thickness samples. The second section supports the use of microspheres for indentation experiments, and the last contains the models needed to extract the desired material parameters.

Indentation geometry and force–displacement data

The mechanical properties of linear, isotropic, elastic materials considered here may be completely described by two intrinsic parameters, the Young's modulus E [N/m^2] and the Poisson's ratio v, in addition to geometry. The collected data are in the form $d = f(z)$ where d represents cantilever deflection within an unknown additive constant d_0, and z is the piezo-actuator translation. The useful part of the data are
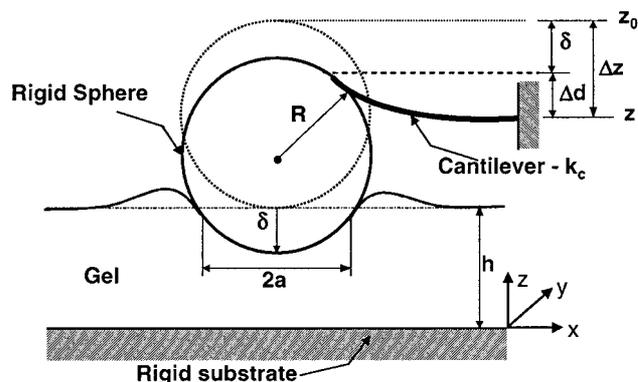

FIGURE 3 Schematic of the indentation experiment. Indentation of a thin sample on a rigid substrate by a spherical probe.

those beyond the contact point, (d_0, z_0), which means that the contact portion of the data are given by

$$\Delta d = f(\Delta z), \quad (2)$$

where $\Delta d = d - d_0$ is the actual cantilever deflection, and $\Delta z = z - z_0$ the corresponding piezo translation, with d and z being the actual measured quantities. Figure 3 is a schematic of the geometry of indentation. It is seen that the piezo translation Δz equals the sum of the cantilever deflection $\Delta d = d - d_0$, and the sample indentation δ,

$$\Delta z = \Delta d + \delta. \quad (3)$$

If k_c[N/m] is the cantilever stiffness, the force deflecting the cantilever, $F = k_c \Delta d$, is transmitted to the sample. Contact mechanics relates this force to the indentation. Because the contact area depends on the force, the relation is nonlinear and can be written in the general form,

$$F = k_c \Delta d = F(\delta; R, h; E, v), \quad (4)$$

where the parameters E and v are the material moduli to be extracted from the experimental data, and R and h are the probe radius of curvature and the sample thickness, respectively. Substitution of δ from Eq. 3 and the introduction of the new variable $w = z - d$, which is a measured quantity, results in an implicit form of Eq. 4,

$$d = d_0 + k_c^{-1}F(w - (z_0 - d_0); R, h; E, v). \quad (5)$$

The right-hand side of this equation is a generally complex relation among the various geometric and material parameters of the problem and is derived by solving the appropriate contact problem. Fitting such a mathematical model to the experimental data gives estimates for unknown parameters such as E and v. For this purpose, the data are also transformed into a form d versus w, so that they conform to the form of the fitting function, Eq. 5. The contact point (d_0, z_0) is sometimes difficult to establish directly from the data, especially for soft samples, so it may also have to be estimated along with the material parameters. In fact, any

subset of the parameter set $\{E, v, d_0, z_0, R, h\}$ may be used as the fitting parameter vector in a parameter-estimation scheme.

The detection of the actual contact point may be possible to within a few nanometers by observing perturbations in the cantilever thermal-noise spectrum as long-range interactions come into play during approach (Heinz et al., 2000; Kosalek et al., 2000). That would depend on the nature of the surface, so some preliminary experimentation may be required. Such capability, however, was not available for our experiments. The usual practice is to truncate the data visually and assume the location of the contact data point and then fit the data by various methods. The errors associated with such an approach and improvements to this method are explored here.

Hertzian contact problem: estimation of sample strains

Small deformations or strains is the most fundamental assumption of the Hertz formulation (Hertz, 1881). Here we show that the assumption is easily violated with sharp pyramidal indenters. Various simple indenter geometries, such as a sphere, a cone, or a paraboloid, can be considered. For small indentations the spherical probe becomes identical to the paraboloid for which the solution exists in closed form. Among all the above profiles, and including the pyramidal profile of the most common AFM silicon nitride tips, the spherical or paraboloid shapes will, in general, generate conditions of lowest stresses and strains. The limits of small strains under a spherical indenter will represent a conservative estimate for the other probe profiles.

The basic formulas of the Hertzian model are given in the first section of the Appendix. We used Eqs. A1–A4 to compute axial strain, $\varepsilon_{zz} = \partial u_z / \partial z$. At the contact point,

the integrations can be performed in closed form, resulting in

$$\varepsilon_{zz}(0, 0) = \frac{2}{\pi} \frac{a}{R} \frac{1}{1 - v}, \qquad (6)$$

where a is the contact radius given by

$$a = \left(\frac{3}{4} \frac{1 - v^2}{E} FR \right)^{1/3}, \qquad (7)$$

and F and R are the indentation force and probe radius, respectively.

Some indicative results for the maximal strain are shown in Fig. 4 for three values of the Young's modulus, 1, 5, and 20 kPa. These are values in the range typical of biological tissue such as cells. Notice that, for radii of curvature of the probe that are typical of the commercial silicon-nitride probes ($\leq$100 nm), the strains for forces down to a few pico-Newtons are much larger than 20%, which is viewed as the upper limit before material nonlinearity invalidates linear elasticity theory. For example, a 100-nm radius of curvature, which represents a moderately blunt tip, will result in strains that are too large even for a force of 1 pN. Moreover, even with the softest cantilevers available, the lower limit of a measurable force is of the order of several pico-Newtons.

The above computations point to the following conclusions. First, the use of the commercially available probes on soft biological samples will inevitably lead to erroneous estimates of material parameters. Strains such as those shown above, when probing live cells, for example, may be forcing lateral lipid flow resulting in membrane penetration of the tip. In that case, the material parameters estimated by the simple Hertzian contact theory may bear no relation to the apparent material properties exhibited by cells in vivo and under physiological conditions. If a large enough radius of curvature is used, however, it should be possible to apply forces that induce reasonable strains and hence allow reliable extraction of relevant material parameters. Besides, for many physiologic in vivo situations, mechanically induced strains are relatively small, and that is the case of interest. In cases where very large strains develop, the parameters E and v are no longer meaningful.

The need for simplicity and robustness in experimental procedures supports the use of the spherical indenter geometry because it is the one that will cause the smallest stress and strain concentrations. Also, the well-defined geometry lends credence to the mathematical models that are used for parameter extraction. From the values shown in Fig. 4, one can see that a radius of 5 μm ensures that strains will be kept in the linear region even for relatively large forces. Consideration should be given to the consequent loss of resolution because of the large radius of curvature. Typically the area of contact will approximately
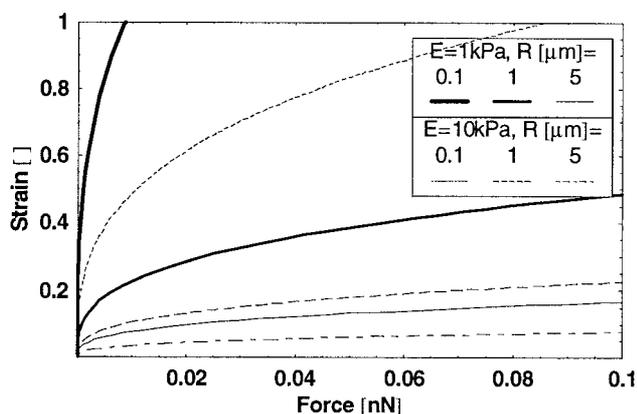

FIGURE 4 Computed maximal strains for different materials and indenter probe radii of curvature.

be a circle of diameter of about a micron, which defines the resolution, but that should not be a major drawback when measuring whole cells. The measurement of molecular structures, in contrast, where resolution is paramount, does not present the same difficulties because of the usually much higher effective stiffness.

Finite thickness sample models

The few theoretical models that exist for finite thickness samples are inconvenient because they require extensive numerical computations that prohibits their use for routine analysis of force–displacement curves, and mapping of elastic properties over an extensive area of a sample. Another difficulty is the need to know the actual sample thickness. This, however, may often be easily overcome in AFM measurements by performing an initial topographic scan of the sample. For thin samples (≤ 5 µm), commercial AFM scanners possess the vertical range needed for the task.

We present two approaches for correcting for the finite thickness of the samples. In the first, we construct an approximate solution using the method of images for the case where the sample is not bonded to the supporting substrate. In the second, we first derive the Green's function for a finite thickness sample bonded to the substrate and use that to compute approximate indentations. In both approaches, the integral equations are satisfied by a computed, effective pressure profile acting on the Hertzian contact area. The details of the mathematical development are presented in the Appendix. The results are summarized in the final relation between the applied force F and the indentation δ,

$$F = \frac{4E}{3(1 - v^2)} R^{1/2} \delta^{3/2} \left[1 - \frac{2\alpha_0}{\pi} \chi + \frac{4\alpha_0^2}{\pi^2} \chi^2 \right.$$
$$\left. - \frac{8}{\pi^3} \left(\alpha_0^3 + \frac{4\pi^2}{15} \beta_0 \right) \chi^3 + \frac{16\alpha_0}{\pi^4} \left(\alpha_0^3 + \frac{3\pi^2}{5} \beta_0 \right) \chi^4 \right], \quad (8)$$

where $\chi = \sqrt{R\delta}/h$, and the constants α_0 and β_0 are functions of the material Poisson's ratio v given below. Notice that the term outside the bracket represents the Hertz solution for the indentation of a semi-infinite solid and the terms inside the bracket are corrections needed to account for the finite thickness of the actual sample. As expected, the latter vanish as h becomes large. It is clear from this expression that, as the sample becomes thinner, the force required to cause a given indentation increases. This is the apparent stiffening effect that has been widely observed experimentally. A positive feature of this solution is that it is valid for all values of the Poisson's ratio and, because α_0 is a monotonic function, the apparent stiffness of the sample is maximum for incompressible material. Another feature of Eq. 8

is that it is valid whether the sample is bonded to the substrate or not. The only difference is that the parameters α_0 and β_0 depend differently on v. When the sample is not bonded to the substrate, they are given by

$$\alpha_0 = -0.347 \frac{3 - 2v}{1 - v}, \quad \beta_0 = 0.056 \frac{5 - 2v}{1 - v}, \quad (9)$$

and, when the sample is bonded to the substrate, they are given by

$$\alpha_0 = -\frac{1.2876 - 1.4678v + 1.3442v^2}{1 - v},$$
$$\beta_0 = \frac{0.6387 - 1.0277v + 1.5164v^2}{1 - v}. \quad (10)$$

Notice the linear dependence of the force on Young's modulus and its nonlinear dependence on the Poisson's ratio. Theoretically, it should be possible to extract both E and v, but, for most biological samples, it is safe to assume incompressibility, $v = 0.5$, because of their high water content. In this case, and when the sample is not bonded to the substrate, Eq. 8 can be written as

$$F = \frac{16E}{9} R^{1/2} \delta^{3/2} [1 + 0.884\chi + 0.781\chi^2$$
$$+ 0.386\chi^3 + 0.0048\chi^4], \quad (11)$$

and, when the sample is bonded,

$$F = \frac{16E}{9} R^{1/2} \delta^{3/2} [1 + 1.133\chi + 1.283\chi^2$$
$$+ 0.769\chi^3 + 0.0975\chi^4]. \quad (12)$$

The above relations agree with the intuitive notion that the same sample appears stiffer when bonded to the substrate than when it is allowed to slip. The difference is large enough to be a consideration and becomes more significant as the layer thickness decreases. This agrees with the theoretical findings in the asymptotic solutions for a flat-ended circular indenter derived previously (Yang, 1998) and the recent results for a spherical indenter (Chadwick, 2002).

Parameter estimation can be performed after the above equations are cast in the form of Eq. 5 where the indentation δ is written in terms of the initial contact point (d_0, z_0). In the commonly used estimation method, the contact point is visually chosen and the model equation solved for E for each data point. If it is assumed that small errors are made in d_0 and z_0, Δd_0 and Δz_0, respectively, and that the Young's modulus is estimated by inverting either the Hertzian or the
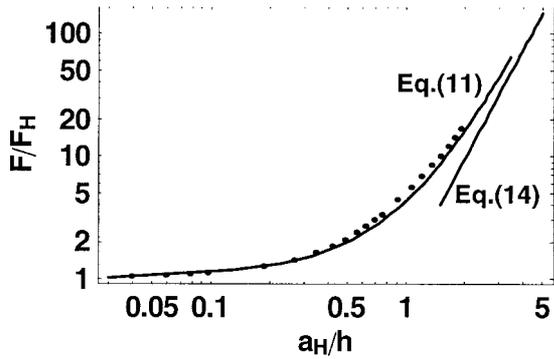
FIGURE 5 Comparisons between present theories and numerical results. The circular dots indicate values derived from all the tabulated data in Hayes et al. (1972).
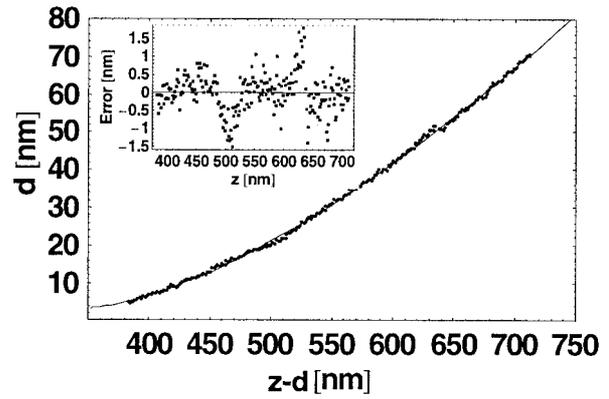

FIGURE 6 Least squares fit of AFM data collected on a thick gel using a 2-μm sphere. Insert shows the residual error distribution.

finite thickness models, Eq. 8, to match data point (d_i, w_i), the resulting estimate may be written, to first order, as

$$\frac{\Delta E_i}{E} = \frac{\Delta d_0}{d_i - d_0} - \frac{\Delta(z_0 - d_0)}{w_i - (z_0 - d_0)} \left(2 - \frac{\pi}{2(\pi - 2\alpha_0\chi_0)} \right),$$

(13)

where E and χ_0 are the values that would be obtained for the Young's modulus and for χ, respectively, if $(d_0, z_0) = (0, 0)$. For the Hertzian model, $\chi_0 = 0$. Notice that the error ΔE decreases as one uses points further away from the origin, but, for points near the contact point, the results can be very erratic. In contrast, because, in keeping with material linearity, points with too large w and d should not be used either. Therefore, this type of error may often be significant.

Clearly, there is an appropriate range of sample thickness and indentation for any given tip radius for which the above formulas are valid. As the parameter χ is increased with smaller sample thickness, the asymptotic series expansion may loose accuracy. Let us assume that, to maintain material linearity, the maximum total strain should never exceed 10%, or $\delta \leq 0.1$ h. If it is agreed that the correction is significant if the first term of the series adds at least 10% to the force, then $1.133\chi \geq 0.1$. This translates to $h \leq 12.8R$. For sample thicknesses greater than this, one may use the semi-infinite sample assumption safely. For the series to converge, in contrast, one may roughly set an upper bound of $\chi \leq 1$ which translates to $h \geq 0.1R$. For thinner thicknesses, the series does not represent the physics of the

problem and may not be safe to use. Instead, the equations derived in Chadwick (2002) and given below should be used:

For bonded sample:

$$F = (2\pi/3)ER^{1/2}\delta^{3/2}\chi^3,$$

(14)

For nonbonded sample:

$$F = (2\pi/3)ER^{1/2}\delta^{3/2}\chi.$$

(15)

Notice the striking difference in the dependence of the force on the sample thickness for given R and indentation.

To summarize the ranges of validity of Eqs. 11–12 and 14–15, it is useful to make comparisons with a more exact, numerical solution in the literature. For that purpose, the results presented in Hayes et al. (1972) were found to be the most appropriate. The comparison is made in Fig. 5, where the ratio F/F_H is plotted versus a_H/h where the subscript H denotes "Hertz" and refers to the force and contact radius for the case of an infinitely thick sample and for the same R and δ. Notice that the agreement is surprisingly good even up to $a/a_H \approx 1$
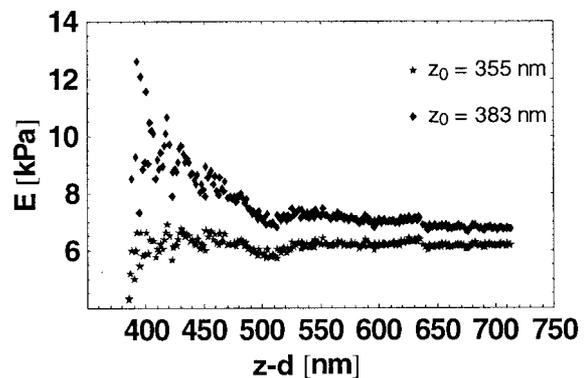

FIGURE 7 Estimation of E by fitting each data point independently to Eq. 12 after determination of the contact point. The lower curve corresponds to a contact point as determined by the least squares fit of Fig. 6. The upper curve corresponds to a contact point determined visually.

TABLE 1 Comparisons between macroscopic and AFM measurements using different probe tips on thick gels

PVA concentration, 1.6%	Measurement Method			
	AFM			
	Sharp tip	$R = 2$ μm	$R = 5$ μm	Macroscopic
Young's modulus, E [kPa]	8.2 ± 1.3	5.2 ± 0.8	5.4 ± 0.9	5.9

and that the asymptotic behavior of Eq. 11 has the correct slope even for very thin samples. This means that the rough limit estimated above ($h \geq 0.1R$) for the use of Eq. 11 is rather conservative. For $F/F_{\mathrm{H}} \gtrsim 100$, however, Eqs. 14–15 should be used.

RESULTS AND DISCUSSION

The first measurements were performed on thick gels. The results from both microscopic and macroscopic measurements are given in Table 1. The macroscopic measurements were performed on two samples, and the Young's modulus estimate represents a mean value over the sample volume. The AFM measurements were performed at a number of different locations (generally 5–15 different randomly chosen locations). The mean values and standard deviation of the estimates of E are included in the table.

It is seen that AFM measurements using the standard sharp tip result in higher estimates of the Young's modulus. The accuracy when using microspheres of either 2- or 5-μm radius as the probe tip, is excellent. The variability observed in data from different points across the gel surface is an indication of microscopic gel inhomogeneities. Also, when using sharp tips, the error is more difficult to characterize because the radius of curvature is really unknown unless separate estimation of its radius is made by imaging dimensionally known objects. For example, a probe radius of curvature that is in error by a factor of 2 will result in a 41% error in the Young's modulus for thick samples and even larger for thin samples. Figure 6 shows the least squares fit for a representative force–displacement curve along with the error residuals of the fit. For the case shown, the maximum contact radius is of the order of 300–400 nm. Although the overall quality of fit is rather good, the fitting residuals exhibit systematic structure, which may be reflecting the microstructure observed in the electron micrograph of Fig. 1. Apparent 150-nm gaps in the gel matrix may cause the force–distance curves to deviate from the smooth function expected from a truly homogeneous material. In addition, these gaps would have an unpredictable effect on the force–distance curves obtained using sharp tips. A sharp tip could easily disrupt the gel matrix locally or probe inside a large gap.

Figure 7 shows the results of the method where the contact point is chosen and each data point is fit to the contact model to estimate E. Results are shown for two choices of the contact point. It is seen that even small errors in choosing the contact point biases the results, but the resulting error in the estimate of the Young's modulus can be significant even for such thick samples.

Thin gels were prepared from polymer solutions at three different polymer concentrations. Thick samples made from the same solutions were used to measure their Young's moduli macroscopically. Force–displacement data were collected from the thin samples and analyzed according to

the methods described here. The results are summarized in Table 2. The AFM indentation experiments were performed at a number of locations within a region of a few micrometers, and microscopic gel inhomogeneity was also evident. The results show that, when using sharp tips either in conjunction with the Hertz model or with our finite thickness correction, the estimation error in E is significant. For the softest gel, the standard deviation was so large and the quality of the fits was so poor as to render the results meaningless. Moreover, correcting for the finite thickness results in significant improvement even when using the sharp tips. When using 2- or 5-μm spheres in conjunction with the models corrected for finite thickness, the estimated value of E is very close to that obtained by macroscopic measurements.

Figure 8 shows the least-squares fit for a representative data set. The data were fitted using the finite thickness model for bonded sample and the Hertzian model. It is seen that the quality of fit for the finite thickness model is excellent but the Hertzian model fit is significantly inferior. In the same figure, we show the error residuals for fitting with the two models. The larger and more systematic residuals in the Hertzian fit indicate the inappropriateness of the Hertzian model for such thin samples.

In Fig. 9, using the same data as shown in Fig. 8, the Young's modulus is estimated by fitting each data point independently after the determination of the initial contact point. In the same plot, the Hertzian and the finite thickness models are compared for two different choices of the contact point. Notice that errors in the contact point result in an estimate of E that decays for larger w_i, which is consistent with the error derived in Eq. 13 showing algebraic decay of the error. Also, the incorrect contact point will result in a significant flat region of the curve resulting from the finite thickness model but that plateau will be in error.

The results obtained here confirm that it is possible to estimate elastic moduli of soft samples from AFM data that closely agree with macroscopically measured values, provided microspheres are used as the measuring probes (Mahaffy et al., 2000). Also, the results consistently support the corrections developed here to the Hertzian indentation model for finite thickness samples. In parallel, the inappropriateness of using AFM probes with sharp tips for thin, soft samples has been demonstrated. Nevertheless, as the results in the first row of Table 2 demonstrate, even if probes with sharp tips were to be used, it is important to correct for thickness. We have here derived corrections to the Hertz model for finite thickness that cover the full range of forces, tip radii, and sample thicknesses. The derived corrections are simple expressions and, as such, add no significant complexity in the methods for extracting elastic moduli. We have

TABLE 2 Young's moduli estimates in kPa

| | Measurement Method | | | | |
| | AFM Measurements | | | | |
Concentration/thickness	Sharp tip Hertz model	$R = 2 \mu m$	$R = 5 \mu m$	Sharp Tip	Macroscopic
1%/1.75 μm	>30	3.1 ± 0.1	3.7 ± 0.4	>50	2.73
1.9%/2.4 μm	24.9 ± 0.5	9.4 ± 0.1	8.8 ± 0.6	11.2 ± 0.2	7.80
3.3%/2.7 μm	76.1 ± 3.7	24.2 ± 2.0	19.4 ± 3.1	30.1 ± 2.4	20.34

Macroscopic versus AFM estimates based on measurements performed on very thin, soft gels. All AFM data were fit with the thickness-corrected model except the left-most column where the Hertz model was used.
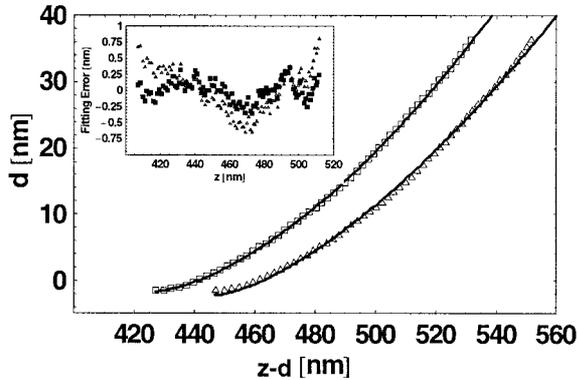

FIGURE 8   Least squares fit of data collected on a very thin gel (2.7 μm) using a 2-μm sphere. The same data are shown twice, with the curve to the right shifted horizontally by 20 nm for clarity. The data are fit using the Hertzian model (*open squares*) and the bonded finite thickness model (*open triangles*). Insert shows the corresponding residual errors of the fits. Estimated values for E were 21.53 (thickness corrected) and 26.48 kPa (Hertz). Corresponding root mean square errors for the fits were 0.16 and 0.36 nm.

also demonstrated that the problem of determining the contact point on soft samples can be effectively handled within the parameter estimation scheme.
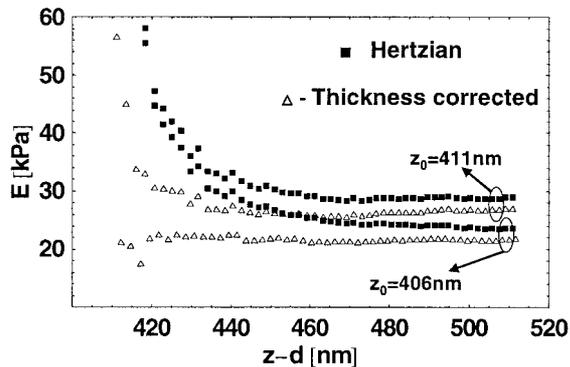

FIGURE 9   Young's modulus estimation by fitting each data point independently after choosing the contact point. The lower two curves correspond to the contact point estimated from least squares fitting ($z_0 = 406$ nm). The other two curves correspond to a contact point that was three data points to the right of the previous one ($\Delta z_0 \sim 5$ nm).

APPENDIX

Hertzian theory

The analysis follows the approach used by Landau and Lifshitz (1959). Let us assume a spherical probe of radius R applies a total force F in the negative z direction, distributed over the contact circle of radius a. The force is applied at the free surface ($z = 0$) of a semi-infinite solid and is centered at $r = 0$, where r is the in-plane radial distance in the $z = 0$ plane. The axial displacement field u_z, may be written in terms of the pressure distribution P_z and the Green's function G

$$u_z(\mathbf{r}, z) = \iint_A P_z(r_s) G(s) \, dA, \qquad (A1)$$

where A is the contact region, and the Green's function is the displacement profile for a point force,

$$G(s) = -\frac{1 + v}{2\pi E s}\left(\frac{z^2}{s^2} + 2(1 - v)\right), \qquad (A2)$$

and the Hertz pressure field applied by the sphere is

$$P_z(r_s) = p_0 \sqrt{a^2 - r_s^2}, \qquad (A3)$$

where $s = |\mathbf{r}| = (r^2 + r_s^2 - 2rr_s \cos \theta + z^2)^{1/2}$ is the distance between source (r_s, 0, 0) and observation point (r, θ, z); θ and z are their angular and vertical distances, respectively, and $p_0 = 2E/\pi R(1 - v^2)$. The contact radius, a, is given in terms of the applied force and the sample material parameters,

$$a = \left(\frac{3}{4}\frac{1 - v^2}{E} FR\right)^{1/3}. \qquad (A4)$$

A finite thickness layer resting on a rigid substrate: method of images

Let us assume a sample of thickness h extending in the x–y plane and resting onto a rigid substrate located at $z = -h$. A spherical probe applies a force F at the origin in the negative z direction. We construct an equivalent problem by combining multiple images of the actual probe in such a way as to satisfy all the boundary conditions of the original problem. The model is shown in Fig. A1, where it is explained that an infinite number of images is required. Each of the images is assumed to apply the force to a semi-infinite sample for which the solution is known. We assume that the rigid boundary modifies the semi-infinite solution by altering the pressure distribution across the contact area. We use the known solutions from each image to construct the pressure profile in the presence of the rigid boundary.

Let s be the in-plane distance between source and observation points, $s^2 = r^2 + r_s^2 - 2rr_s \cos\theta$. Because the images act on planes located at vertical distances that are multiples of $2h$ from the actual sample free surface, one can write a general expression for the part of the Green's function that results from the general image at $z = 2nh$, $n = 0, 1, 2, \ldots$,

$$G_n(s) = (-1)^n \frac{1+v}{2\pi E} \left\{ \frac{z^2}{(s^2 + z^2)^{3/2}} + \frac{2(1-v)}{(s^2 + z^2)^{1/2}} \right\}\Bigg|_{z=2nh},$$

$$n = 0, 1, 2, \ldots. \quad (A5)$$

And the complete Green's function for the array of images will be

$$G_T(s) = \sum_{n=0,\pm1,\pm2,\ldots} G_n(s). \quad (A6)$$

This is the Green's function for the deformation of the finite thickness sample free surface. In this model, the sample surface that is in contact with the rigid substrate is free to slide horizontally. Because, ultimately only the probe contact region at the surface sample is of interest, it is justified to assume that $s \le h$, especially if the sample thickness is not much smaller than the probe radius of curvature. This allows the Taylor series expansion of the Green's function, which may also be written in terms of the small parameter, $\varepsilon = \delta/h$, where δ is the indentation at the center of the contact area, which will be referred to as the "indentation"

$$G_T(s) = G_\infty(s)(1 + \varepsilon\alpha(s) + \varepsilon^3\beta(s) + \varepsilon^5\gamma(s) + \cdots), \quad (A7)$$

where $G_\infty(s) = G_0(s) = [(1-v^2)/\pi E](1/s)$ is the Green's function for the surface indentation of a semi-infinite sample, whereas the higher order terms are corrections due to the finite sample thickness. The coefficients of the series are simple functions of the Poisson's ratio of the sample material,

$$\alpha(s) = \alpha_0(v)\frac{s}{\delta},$$

$$\beta(s) = \beta_0(v)\left(\frac{s}{\delta}\right)^3, \quad (A8)$$

$$\gamma(s) = \gamma_0(v)\left(\frac{s}{\delta}\right)^5,$$

where the coefficients $\alpha_0(v)$, $\beta_0(v)$, and $\gamma_0(v)$ are

$$\alpha_0(v) = -0.347\frac{3-2v}{1-v},$$

$$\beta_0(v) = 0.056\frac{5-2v}{1-v}, \quad (A9)$$

$$\gamma_0(v) = -0.011\frac{7-2v}{1-v}.$$

Assuming a spherical probe and that no significant long range interactions take place, it is safe to assume that the indentation will conform to the shape of the probe so that one may write

$$\delta - \frac{r^2}{2R} = \iint_A P(r_s)G_T(s)\,dA, \quad (A10)$$

where $P(r_s)$ is the pressure profile applied by the spherical probe. Because we know the Green's function, Eq. A10 is an integral equation for the pressure profile. The approach taken here assumes that the contact radius is independent of sample thickness and that the pressure profile is modified by the presence of the rigid substrate. Therefore, it is reasonable to assume that the pressure profile will be a function of the same small parameter ε ($= \delta/h$) and it may then be expanded in terms of ε as was done with the Green's function

$$P(r_s) = P_\infty(r_s) + \varepsilon P_1(r_s) + \varepsilon^2 P_2(r_s) + \varepsilon^3 P_3(r_s) + \cdots. \quad (A11)$$

Substitution of Eqs. A7 and A11 into Eq. A10 and rearrangement results in a series of integral equations for P_∞, P_1, P_2, P_3, etc. The first-order problem has exactly the form of the Hertz problem of indenting a semi-infinite sample with a rigid spherical probe and the pressure profile is given by (Landau and Lifshitz, 1959)

$$P_\infty(r_s) = \frac{2E}{\pi(1-v^2)}\frac{1}{R}\sqrt{a_0^2 - r_s^2}. \quad (A12)$$

This relation can be derived by substituting the form $p_0(a_0^2 - r_s^2)^{1/2}$ into the first-order integral equation and solving for p_0 and a_0. The contact radius turns out to be simply related to the indentation δ and the probe radius of curvature R,

$$a_0^2 = R\delta. \quad (A13)$$

The second-order problem results in

$$\iint_A G_\infty(s)P_1(r_s)\,dA = -\iint_A G_\infty(s)P_\infty(r_s)\alpha(s)\,dA$$

$$= -\frac{4\alpha_0}{3\pi}\frac{a_0^3}{R\delta}, \quad (A14)$$

because the right-hand side integral can be performed closed-form. This equation has the same form as that obtained for indenting an infinitely thick sample with a flat-ended cylindrical punch, which accepts a solution of the form $P_1 = p_1/(a_0^2 - r_s^2)^{1/2}$ (Johnson, 1985). Integration of the first integral in Eq. A14 allows the calculation of the factor p_1 so that

$$P_1 = -\frac{4\alpha_0}{3\pi^2(1-v^2)}\frac{Ea_0^3}{R\delta}\frac{1}{\sqrt{a_0^2 - r_s^2}}. \quad (A15)$$

The next-order problem has a form and a solution similar to the one for P_1,

$$P_2(r_s) = \frac{8E\alpha_0^2}{3(1-v^2)\pi^3}\frac{a_0^4}{R\delta^2}\frac{1}{\sqrt{a_0^2 - r_s^2}}. \quad (A16)$$

The fourth-order expansion term results in the integral equation,

$$\iint_A G_\infty(s)P_3(r_s)\,dA$$

$$= -\iint_A G_\infty(s)[P_2(r_s)\alpha(s) + P_\infty(r_s)\beta(s)]\,dA$$

$$= -\frac{4}{3\pi}\frac{a_0^3}{R\delta^3}\left[\left(\frac{4\alpha_0^3}{\pi^2} + \frac{2\beta_0}{5}\right)a_0^2 + \beta_0 r^2\right]. \quad (A17)$$
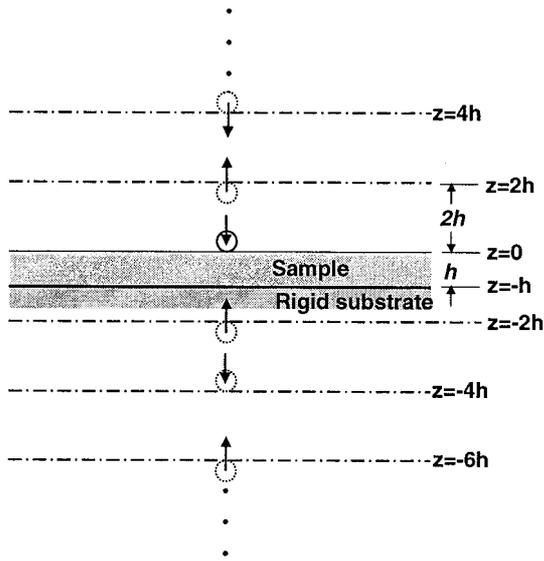
FIGURE A1 An infinite sequence of images of the spherical probe satisfies all the boundary conditions for the finite thickness sample. All images act on semi-infinite samples and in the direction indicated by the arrows. The first ($z = -2h$) image satisfies the rigid interface ($z = -h$) boundary condition (with no bonding), but results in a net stress on the free surface of the finite thickness sample. That stress is eliminated by the second image source ($z = 2h$) which, however, violates the rigid interface boundary condition ($z = -h$). This necessitates the next image ($z = -4h$), and so on, ad infinitum and with the degree of boundary condition violation decreasing with every pair of images because they are further removed from those boundaries.

A pressure profile of the form,

$$P_3(r_s) = \frac{p_{31}}{\sqrt{a_0^2 - r_s^2}} + \frac{p_{32}r_s^2}{\sqrt{a_0^2 - r_s^2}}, \qquad (A18)$$

would satisfy this integral equation. The unknown factors p_{31} and p_{32} are calculated by substituting Eq. A18 into A17. Finally,

$$P_3(r_s) = -\frac{16}{15\pi^4} \frac{E}{1 - v^2} \frac{a_0^3}{R\delta^3}$$

$$\times \frac{[(5\alpha_0^3 - 2\pi^2\beta_0)a_0^2 + 5\pi^2\beta_0 r_s^2]}{\sqrt{a_0^3 - r_s^2}}. \qquad (A19)$$

The next higher-order problem is similar to the previous one and its solution takes the form,

$$P_4(r_s) = \frac{32}{45\pi^5} \frac{E\alpha_0}{1 - v^2} \frac{a_0^4}{R\delta^4}$$

$$\times \frac{[(15\alpha_0^3 - \pi^2\beta_0)a_0^2 + 15\pi^2\beta_0 r_s^2]}{\sqrt{a_0^2 - r_s^2}}. \qquad (A20)$$

The force–displacement relation can now be derived from the fact that the corrected pressure profile must integrate to the total applied force. When

the series expansion for the pressure profile is integrated within the contact region and the contact radius is substituted from Eq. A13, the final result can be written as

$$F = \frac{4E}{3(1 - v^2)} R^{1/2}\delta^{3/2} \left[1 - \frac{2\alpha_0}{\pi}\chi + \frac{4\alpha_0^2}{\pi^2}\chi^2 \right.$$

$$- \frac{8}{\pi^3}\left(\alpha_0^3 + \frac{4\pi^2}{15}\beta_0\right)\chi^3$$

$$\left. + \frac{16\alpha_0}{\pi^4}\left(\alpha_0^3 + \frac{3\pi^2}{5}\beta_0\right)\chi^4 \right], \quad (A21)$$

where $\chi = \sqrt{R\delta}/h$. This is the final force versus indentation relation valid for finite thickness samples. Notice that the term outside the brackets has the Hertzian form, whereas the terms inside the brackets are corrections due to the finite thickness.

Finite thickness layer bonded to a rigid substrate: integral transform method

Sneddon (1965) and Dhaliwal and Rau (1970) used integral transform methods to solve the axisymmetric problem for a semi-infinite- and finite-thickness elastic layer, respectively. For the finite-thickness sample, where the interest lies here, they derived an integral equation whose solution required extensive numerical computations. Here, we take a slightly different approach and first compute the Green's function for a finite-thickness solid. This casts the problem in a simpler framework in which we can follow the procedure in the previous section to derive an explicit expression for the force versus indentation relation.

The basic equations are given in some detail in (Dhaliwal and Rau, 1970) but the main idea is to use the linear elasticity equations for an axisymmetric problem in a cylindrical coordinate system,

$$\mu\nabla^2\mathbf{U} + (\lambda + \mu)\nabla(\nabla \cdot \mathbf{U}) = 0,$$

$$\sigma_{zz}(r, z) = (\lambda + 2\mu)\partial_z u_z + \lambda\left(\partial_r u_r + \frac{u_r}{r}\right), \quad (A22)$$

$$\sigma_{rz}(r, z) = \mu(\partial_z u_r + \partial_r u_z),$$

where $\mathbf{U} = \{u_r, 0, u_z\}$ is the displacement vector, σ_{ij} are stresses, and $\lambda = 2\mu v/(1 - 2v)$ and $\mu = E/(2(1 + v))$ are the Lamé constants. The general solution of the above system can be written as

$$2\mu u_r(r, z) = \partial_r\Psi + z\partial_r\Omega \qquad (A23)$$

$$2\mu u_z(r, z) = \partial_z\Psi + z\partial_z\Omega - (3 - 4v)\Omega,$$

where Ψ and Ω are harmonic functions known as the Boussinesq–Papkovitch potential functions (Green and Zerna, 1968). Axisymmetric harmonic functions in the Hankel transform domain have the form

$$\Psi(r, z) = \mathbf{H}_0[A(\zeta)e^{-\zeta z} + B(\zeta)e^{\zeta z}], \qquad (A24)$$

$$\Omega(r, z) = \mathbf{H}_0[C(\zeta)e^{-\zeta z} + D(\zeta)e^{\zeta z}],$$
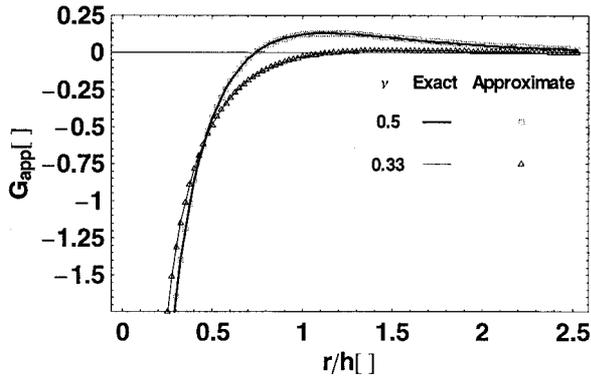
FIGURE A2 The approximate Green's function obtained by inverse transforming Eq. A29 compared to the exact function, which is computed by numerically inverting Eq. A27.

where the transform of order n is defined by

$$f(r, z) = \mathbf{H}_n[\tilde{f}(\zeta, z)] = \int_0^\infty \zeta \tilde{f}(\zeta, z) J_n(r\zeta) \, d\zeta, \quad \text{(A25)}$$

with $J_n(\zeta)$ being the Bessel function of order n. The coefficients A, B, C, and D are determined from the boundary conditions. The boundary conditions for the computation of the Green's function are

$$\sigma_{rz}(r, 0) = 0, \quad \sigma_{zz}(r, 0) = -\frac{1}{\pi} \delta(r), \quad \text{(A26)}$$

$$u_r(r, -h) = 0, \quad u_z(r, -h) = 0,$$

where $\delta(r)$ is the Dirac delta function. These conditions suffice to calculate the unknown constants in Eq. A24, which, in turn, allows the transformed axial displacement at the free surface to be written as

$$\tilde{u}(\zeta, 0) =$$

$$-\frac{(1 - v)((3 - 4v)(1 - e^{4x}) + 4xe^{2x})}{2\mu\pi\zeta((3 - 4v)(1 + e^{4x}) + 2(5 - 12v + 8v^2 + 2x^2)e^{2x})},$$

(A27)

where $x = h\zeta$. The actual Green's function, which is the axial displacement field caused by a point force, is given by the inverse transform of the above expression. Because the inversion cannot be performed closed-form, an approximate form of the above expression is constructed by least squares, fitting the simpler form

$$\zeta \tilde{u}_z(\zeta, 0) \cong a_0 + (b_0 + c_0 x + d_0 x^2 + e_0 x^3) e^{-2x}, \quad \text{(A28)}$$

which, as it turns out, can approximate the actual function extremely well. The inverse zeroth-order Hankel transform of the above expression is the approximate form of the Green's function,

$$G_{app}(r, 0) = \frac{q_0 h}{r} + \frac{q_1 h^6 + q_2 h^4 r^2 + q_3 h^2 r^4 + q_4 r^6}{(4h^2 + r^2)^{7/2}},$$

(A29)

where the coefficients q_i are algebraic functions of the Poisson's ratio. The numerically inverse transform of the exact expression, Eq. A27, was compared to the approximate form Eq. A29 for values of the Poisson's ratio between 0.3 and 0.5. Errors never exceeded 1–2% of the exact value. A comparison between the exact and the above approximate Green's function is shown in Fig. A2. Therefore, an essentially exact, closed-form expression for the Greens' function for the indentation of a finite-thickness solid has been derived and can now be used to compute the actual indentation caused by a spherical probe. This, again, is equivalent to solving the integral Eq. A10, but using G_{app} instead of G_T. It is clear that the sequence of problems is essentially the same as with the images except the coefficients $\alpha_0(v)$ and $\beta_0(v)$ have a different dependence on Poisson's ratio. In this case, those functional forms are rather complicated but, for the usual range of the Poisson's ratio (0.3–0.5), they can be extremely well fit by the ratio of a quadratic polynomial in v and $(1 - v)$. The fitted forms of $\alpha_0(v)$ and $\beta_0(v)$ are given in Eq. 10.

REFERENCES

A-Hassan, E., W. F. Heinz, M. D. Antonik, N. P. D'Costa, S. Nageswaran, C.-A. Schoenenberger, and J. H. Hoh. 1998. Relative microelastic mapping of living cells by atomic force microscopy. *Biophys. J.* 74: 1564–1578.

Akhremitchev, B. B., and G. C. Walker. 1999. Finite sample thickness effects on elasticity determination using atomic force microscopy. *Langmuir.* 15:5630–5634.

Aleksandrov, V. M. 1968. Asymptotic methods in contact problems of elasticity theory. *Prikl. Mat. Mekh.* 32:672–683.

Aleksandrov, V. M. 1969. Asymptotic solution of the contact problem for a thin elastic layer. *Prikl. Mat. Mekh.* 33:61–73.

Boussinesq, J. 1885. Applications des Potentiels a l'Etude de l'Equilibre et du Mouvement des Solides Elastiques. Gauthier-Villars, Paris.

Burnham, N. A., and R. J. Colton. 1989. Measuring the nanomechanical properties and surface forces of materials using the AFM. *J. Vacuum Sci. Technol.* A7:2906–2913.

Chadwick, R. S. 2002. Axisymmetric indentation of a thin incompressible layer. *SIAM J. Appl. Math.* (in press).

Chen, W. T., and P. A. Engel. 1972. Impact and contact stress analysis in multilayer media. *Int. J. Solids Struct.* 8:1257–1281.

Costa, K. D., and F. C. P. Yin. 1999. Analysis of indentation: implications for measuring mechanical properties with atomic force microscopy. *J. Biomech. Engr. Trans. ASME.* 121:462–471.

Dhaliwal, R. S., and I. S. Rau. 1970. The axisymmetric Boussinesq problem for a thick elastic layer under a punch of arbitrary profile. *Int. J. Engr. Sci.* 8:843–856.

Domke, J., and M. Radmacher. 1998. Measuring the elastic properties of thin polymer films with the atomic force microscope. *Langmuir.* 14: 3320–3325.

Green, A. E., and W. Zerna. 1968. Theoretical Elasticity. Oxford University Press, Oxford, U.K. 163–167.

Haga, H., S. Sasaki, K. Kawabata, E. Ito, T. Ushiki, and T. Sambongi. 2000. Elasticity mapping of living fibroblasts by AFM and immunofluorescence observation of the cytoskeleton. *Ultramicroscopy.* 82: 253–258.

Hayes, W. C., L. M. Keer, G. Herrmann, and L. F. Mockros. 1972. A mathematical analysis for indentation tests of articular cartilage. *J. Biomech.* 5:541–551.

Heinz, W. F., M. D. Antonik, and J. H. Hoh. 2000. Reconstructing local interaction potentials from perturbations to the thermally driven motion of an atomic force microscope cantilever. *J. Phys. Chem. B.* 104: 622–626.

Hertz, H. 1881. Uber die Beruhrung Fester Elastischer Korper (On the Contact of Elastic Solids). *J. Reine Angew. Math.* 92:156–171.

Heuberger, M., G. Dietler, and L. Schlapbach. 1994. Mapping the local Young's modulus by analysis of the elastic deformations occurring in atomic force microscopy. *Nanotechnology.* 5:12–23.

Hoh, J. H., and W. F. Heinz. 1999. Spatially resolved force spectroscopy of biological surfaces using the atomic force microscope. *Nanotechnology.* 17:143–150.

Horkay, F., and M. Nagy. 1980. Elasticity of swollen polyvinyl alcohol and poly(vinyl acetate) networks. *Polymer Bull.* 3:457–463.

Johnson, K. L. 1985. Contact Mechanics. Cambridge University Press, Cambridge, U.K. 93.

Kachar, B., M. Parakkal, and J. Fex. 1990. Structural basis for mechanical transduction in the frog vestibular sensory apparatus: I. The otolithic membrane. *Hearing Res.* 45:179–190.

Kim, M. T. 1996. Influence of substrate on the elastic reaction of films for the microindentation tests. *Thin Solid Films.* 283:12–16.

Kosalek, D. O., W. F. Heinz, M. D. Antonik, A. Baik, and J. H. Hoh. 2000. Probing deep interaction potentials with white noise-driven atomic force microscope cantilever. *Appl. Phys. Lett.* 76:2952–2954.

Landau, L. D., and E. M. Lifshitz. 1959. Theory of Elasticity. Pergamon Press Ltd., Oxford, U.K. 30–36.

Lins, U., M. Farina, M. Kurc, G. Riordan, R. Thalmann, I. Thalmann, and B. Kachar. 2000. The otoconia of the guinea pig utricle: internal structure, surface exposure, and interactions with the filament matrix. *J. Struct. Biol.* 131:67–78.

Mahaffy, R. E., C. K. Shih, F. C. MacKintosh, and J. Käs. 2000. Scanning probe-based frequency-dependent microrheology of polymer gels and biological cells. *Phys. Rev. Lett.* 85:880–883.

Matthewson, M. J. 1981. Axi-symmetric contact on thin compliant coatings. *J. Mech. Phys. Solids.* 29:89–113.

Popov, G. I. 1962. The contact problem of the theory of elasticity for the case of a circular area of contact. *Prikl. Mat. Mekh.* 26:152–164.

Radmacher, M. 1995. Imaging soft samples with the atomic force microscope: gelatin in water and propanol. *Biophys. J.* 69:264–270.

Radmacher, M., M. Fritz, J. P. Cleveland, A. Walters, and P. K. Hansma. 1994. Imaging adhesion forces and elasticity of lysozyme adsorbed on mica with the AFM. *Langmuir.* 10:3809–3814.

Radmacher, M., M. Fritz, C. M. Kacher, J. P. Cleveland, and P. K. Hansma. 1996. Measuring viscoelastic properties of human platelets with the atomic force microscope. *Biophys. J.* 70:556–567.

Radmacher, M., R. W. Tillman, M. Fritz, and H. E. Gaub. 1992. From molecules to cells: imaging soft samples with the atomic force microscope. *Science.* 257:1900–1905.

Reynaud, C., F. Sommer, C. Quet, N. El Bounia, and T. M. Duc. 2000. Quantitative determination of Young's modulus on a biphase polymer system using atomic force microscopy. *Surface Interface Anal.* 30:185–189.

Rotsch, C., F. Braet, E. Wisse, and M. Radmacher. 1997. AFM imaging and elasticity measurements on living rat liver macrophages. *Cell Biol. Intl.* 21:685–696.

Sato, M., K. Nagayama, N. Kataoka, M. Sasaki, and K. Hane. 2000. Local mechanical properties measured by atomic force microscopy for cultured bovine endothelial cells exposed to shear stress. *J. Biomech.* 33:127–135.

Sneddon, I. N. 1951. Fourier Transforms. McGraw Hill Book Company, Inc., New York. 450–486.

Sneddon, I. N. 1965. The relation between load and penetration in the axisymmetric Boussinesq problem for a punch of arbitrary profile. *Int. J. Engr. Sci.* 3:47–57.

Tao, N. J., S. M. Lindsay, and S. Lees. 1992. Measuring the microelastic properties of biological materials. *Biophys. J.* 63:1165–1169.

Tu, Y.-O., and D. C. Gazis. 1964. The contact problem of a plate pressed between two spheres. *Trans. ASME J. Appl. Mech.* 31:659–666.

Vinckier, M., and G. Semenza. 1998. Measuring elasticity of biological materials by atomic force microscopy: a minireview. *FEBS Lett.* 430:12–16.

Yang, F. 1998. Indentation of an incompressible elastic layer. *Mech. Materials.* 30:275–286.